

# **On the role of Mn(IV) vacancies in the photoreductive dissolution of hexagonal birnessite**

**Kideok D. Kwon<sup>1\*</sup>, Keith Refson<sup>2</sup>, and Garrison Sposito<sup>1</sup>**

<sup>1</sup>Geochemistry Department, Earth Sciences Division, Lawrence Berkeley National Laboratory, Berkeley, CA 94720

<sup>2</sup>STFC Rutherford Appleton Laboratory, Didcot, Oxfordshire OX11 0QX, United Kingdom

\*Corresponding author: [kkwon@nature.berkeley.edu](mailto:kkwon@nature.berkeley.edu)

## **Abstract**

Photoreductive dissolution of layer type Mn(IV) oxides (birnessite) under sunlight illumination to form soluble Mn(II) has been observed in both field and laboratory settings, leading to a consensus that this process is a key driver of the biogeochemical cycling of Mn in the euphotic zones of marine and freshwater ecosystems. However, the underlying mechanisms for the process remain unknown, although they have been linked to the semiconducting characteristics of hexagonal birnessite, the ubiquitous Mn(IV) oxide produced mainly by bacterial oxidation of soluble Mn(II). One of the universal properties of this biogenic mineral is the presence of Mn(IV) vacancies, long-identified as strong adsorption sites for metal cations. In this paper, the possible role of Mn vacancies in photoreductive dissolution is investigated theoretically using quantum mechanical calculations based on spin-polarized density functional theory (DFT). Our DFT study demonstrates unequivocally that Mn vacancies significantly reduce the band-gap energy for hexagonal birnessite relative to a hypothetical vacancy-free MnO<sub>2</sub> and thus would increase the concentration of photo-induced electrons available for Mn(IV) reduction upon illumination of the mineral by sunlight. Calculations of the charge distribution in the presence of vacancies, although not fully conclusive, show a clear separation of photo-induced electrons and holes, implying a slow recombination of these charge-carriers that facilitates the two-electron reduction of Mn(IV) to Mn(II).

## 1. INTRODUCTION

Photochemical reduction of Mn(IV) oxides by sunlight to form soluble Mn(II) is widely accepted as a principal process whereby Mn is maintained in dissolved form to supply aquatic species in the euphotic zones of marine and freshwater ecosystems (Sunda et al., 1983; Landing and Bruland, 1987; Sunda and Huntsman, 1988, 1990, 1994; Waite et al., 1988, 1993; Matsunaga et al., 1995; Spokes and Liss, 1995; Morgan, 2000; Guipeng et al., 2003; Delgadillo-Hinojosa et al., 2006). Photoreduction of Mn oxides also impacts the solubility of environmentally-important trace elements that are adsorbed by these minerals (Tebo et al., 2004). Most Mn oxides found in natural waters are produced by the bacterial oxidation of soluble Mn(II) (Morgan, 2000; Tebo et al., 2004), which is highly favored kinetically over abiotic oxidation. Recent studies utilizing X-ray absorption spectroscopy and X-ray diffraction have revealed the crystal structures of Mn oxides precipitated by three well-characterized bacteria: the marine species, *Bacillus sp.* strain SG-1 (Bargar et al., 2005; Webb et al., 2005), and two freshwater species, *Leptothrix discophora* (Saratovsky et al., 2006) and *Pseudomonas putida* (Villalobos et al., 2003, 2006). All of the Mn oxides investigated have been found to be layer-type MnO<sub>2</sub> [birnessite (Villalobos et al., 2003)] with hexagonal site symmetry and significant structural disorder resulting from cation vacancies and random sheet-stacking.

Yang et al. (2003) have reviewed the considerable evidence for photo-enhanced dissolution of Mn oxides in the presence of organic reductants (e.g., humic substances) and sunlight, noting, however, that “the mechanism of photoreductive dissolution of MnO<sub>x</sub> is still not clear”. In particular, Mn oxide itself has been suggested to be the chromophore in the photoreaction because of its semiconducting electronic structure. Following this line of reasoning, Sherman (2005) applied oxygen K-edge X-ray spectroscopy to characterize the photoreductive

dissolution of birnessite by the excitation of electrons across a semiconductor band gap, from the electron-occupied valence band (VB, mainly O-2*p* states in birnessite) to the unoccupied conduction band (CB, mainly Mn-3*d* states). If the incident photon energy is greater than the band gap, electrons are excited to the CB and positively-charged holes are created in the VB. To promote electron excitation under illumination by visible light, the band gap must be less than about 3.1 eV ( $\lambda > 400$  nm incident photon wavelength). Electrons in the CB then could reduce structural Mn(IV) to Mn(III) or Mn(II), the latter of which can readily detach into solution, while holes in the VB could oxidize water molecules or nearby organic matter, an effective hole-scavenger which prevents electron-hole recombination.

Sherman (2005) determined a band gap of 1.8 eV from O K-edge X-ray absorption and emission spectra of a well-crystallized synthetic birnessite having triclinic symmetry, interpreting his data under the assumption that band gap excitation corresponds to a ligand-to-metal charge-transfer transition, O-2*p* to Mn-3*d*. Using the Nernst equation and a p.z.c. value of 2.2, Sherman (2005) estimated the bottom of the CB in triclinic birnessite to lie at -0.16 V (vs. SHE) at the pH value of seawater, which is well below the formal electrode potential for the MnO<sub>2</sub>/Mn<sup>2+</sup> couple under the same conditions (1.23 V vs. SHE). Thus triclinic birnessite should be thermodynamically susceptible to photoreductive dissolution in seawater.

However, hexagonal birnessite, not triclinic birnessite, typifies the Mn oxides found in natural aquatic systems. Hexagonal birnessite possesses Mn(IV) cation vacancies in its edge-sharing octahedral sheets, whereas triclinic birnessite does not (Drits et al., 1997; Silvester et al., 1997). In triclinic birnessite, negative structural charge arises from the substitution of Mn(III) for Mn(IV) (Lanson et al., 2002). In hexagonal birnessite, negative structural charge arises from the presence of the Mn vacancies. These vacancies have been identified as strong adsorption sites for

metals (Manceau et al., 2002, 2007; Villalobos et al., 2005; Toner et al., 2006; Takahashi et al., 2007). However, vacancies in semiconducting materials are also known to improve photochemical reactivity as “self dopants,” mainly by narrowing the band gap (Justicia et al., 2002; Hwang, 2005; Nolan and Elliott, 2006). Therefore, a similar role of a Mn vacancy in enhancing the photochemical reactivity of hexagonal birnessite is possible, and it is this hypothesis that we examine theoretically in the present paper using quantum mechanical calculations based on density functional theory (DFT).

Density functional theory is a powerful methodology for investigating the electronic structures of photoreactive semiconducting materials containing doping elements and vacancies (Asahi et al., 2001; Wang and Doren, 2005; Nolan and Elliott, 2006; Picozzi et al., 2007). Because a number of factors influence semiconductor band gaps [e.g., particle size (Viswanatha et al., 2004)], the effects of a Mn vacancy on electronic structure in hexagonal birnessite, which is typically nanoparticulate (Villalobos et al., 2006), must be deconvoluted from those of other factors, a formidable challenge to current experimental techniques. In DFT simulations one can control the Mn vacancy rate and thus readily isolate vacancy effects from the other factors that affect electronic structure. In the present study, the effects of a Mn vacancy on electronic structure were examined for hexagonal birnessite bearing no vacancy, as well as for birnessites with 0.033 and 0.125 Mn vacancies per octahedron, corresponding to the structural formulas,  $\text{MnO}_2$ ,  $\text{H}_{0.13}[\text{Mn}_{0.967}\square_{0.033}]\text{O}_2$  and  $\text{H}_{0.50}[\text{Mn}_{0.875}\square_{0.125}]\text{O}_2$ , respectively, where  $\square$  denotes a Mn vacancy and the protons compensate the resulting negative structural charge.

## 2. COMPUTATIONAL METHODS

## 2.1. Spin-polarized DFT

All calculations were performed with the CASTEP code (Segall et al., 2002; Clark et al., 2005), which implements DFT in a plane-wave basis set to represent wavefunctions and uses ultrasoft pseudopotentials (Vanderbilt, 1990) to replace strong coulomb potentials between the atomic nuclei and core electrons with weak effective potentials, thus dramatically reducing the number of plane waves required to represent wavefunctions. Under standard approximations to account for electron exchange and correlation, eigenstates and eigenvalues of the Kohn-Sham equations (Kohn and Sham, 1965; Payne et al., 1992) were calculated via efficient self-consistent iterative methods including density mixing (Kresse and Furthmüller, 1996). Electron exchange and correlation were described using the spin-polarized generalized gradient approximation (GGA) with Perdew, Burke, and Ernzerhof functionals (Perdew et al., 1996).

Manganese oxides in general exhibit a variety of magnetic states that couple strongly to structural energetics and, therefore, a spin-polarized treatment is essential for accurate DFT calculations (Singh, 1997; Pask et al., 2001; Balachandran et al., 2003), i.e., electron densities must be calculated separately for spin-up and spin-down orientations. In the present study, all calculations for hexagonal birnessite were performed with spin polarization and exhibited ferromagnetic ordering among Mn ions within a layer. The triangular Mn lattice does not allow an antiferromagnetic spin order because of frustration (Moessner and Ramirez, 2006), resulting in the stabilization of the otherwise higher energy ferromagnetic ordering. Table 1 illustrates the importance of including spin polarization in order to obtain accurate MnO<sub>2</sub> structures by DFT geometry optimization. Without spin polarization, DFT underestimates Mn-Mn and Mn-O distances in vacancy-free hexagonal layer type Mn(IV)O<sub>2</sub> (Section 2.2). Antiferromagnetic alignment between octahedral sheets with ferromagnetic ordering in each sheet was also

examined, but the energy difference found was less than the energy variability in calculations using ferromagnetic alignment (i.e.,  $\ll 1$  meV in the total energy per formula unit). Moreover, band gaps calculated with the antiferromagnetic alignment were identical to those calculated with ferromagnetic ordering.

Ultrasoft pseudopotentials were constructed for Mn and O atoms using the on-the-fly pseudopotential generator implemented in CASTEP. The valence electron configurations were  $3s^2 3p^6 3d^5 4s^2$  for Mn and  $2s^2 2p^4$  for O. In the Mn pseudopotential, the number of non-local projectors was one for each  $s$  state ( $3s$  and  $4s$ ) and two each for the  $3p$  and  $3d$  states. In the O pseudopotential, two non-local projectors each were used for the  $2s$  and  $2p$  states. The core radius of Mn was  $2.3 a_0$  ( $a_0 = 0.52918 \text{ \AA}$  is the Bohr radius), and that of O was  $1.3 a_0$ . The  $q_c$  for KE optimization were set at  $5.5$  and  $6 a_0^{-1}$  for Mn and O, respectively. Pseudopotentials at a 500 eV cut-off energy reproduced well the structure and energy data for MnO calculated with the all-electron method (Pask et al., 2001) (see Appendix EA-1). For H, the Vanderbilt-type pseudopotential in the CASTEP library (version 7.3.2) was used, and the core radius was  $0.8 a_0$ .

## 2.2. Model birnessite structures

Hexagonal vacancy-free Mn(IV)O<sub>2</sub> has not yet been synthesized in the laboratory and, therefore, its structure was modeled based on the Mn and O atomic coordinates for a microcrystalline birnessite prepared by thermal decomposition of KMnO<sub>4</sub> at 800°C (Gaillot et al., 2003). This layer type Mn oxide has space group  $P6_3/mmc$  and a two-layer unit cell with hexagonal lattice parameters  $a = 2.840 \text{ \AA}$  and  $c = 14.031 \text{ \AA}$ . After full relaxation of vacancy-free MnO<sub>2</sub>, a Mn-vacancy was incorporated into its MnO<sub>2</sub> supercells and charge-compensated by coordination of one Mn vacancy at the center of each supercell to four H on the dangling O ions around the vacancy (Fig. 1). Two different vacancy concentrations were modeled, with one Mn

vacancy placed in the 4 x 4 x 1 (31 Mn atoms) and 2 x 2 x 1 (7 Mn atoms) supercells, corresponding to the structural formulas,  $\text{H}_{0.13}[\text{Mn}_{0.967}\square_{0.033}]\text{O}_2$  and  $\text{H}_{0.50}[\text{Mn}_{0.875}\square_{0.125}]\text{O}_2$ , respectively, where  $\square$  represents a Mn vacancy.

### 2.3. Convergence and geometry optimization

In all DFT optimizations, the plane-wave basis sets were expanded to a cut-off energy of 500 eV. For the first Brillouin zone, 6 x 6 x 2 k-point grids (Monkhorst and Pack, 1976) were used without a grid origin offset for vacancy-free  $\text{MnO}_2$ . For  $\text{MnO}_2$  with vacancies, 5 x 5 x 2 and 2 x 2 x 2 k-point grids were used for a 2 x 2 x 1 supercell and a 4 x 4 x 1 supercell, respectively. Tests performed on the 6 x 6 x 2 (vacancy-free  $\text{MnO}_2$ ) and 5 x 5 x 2 (vacancies included) grids with the 500 eV cut-off energy achieved very high convergence of both force (0.01 eV/Å or better) and stress (0.01 GPa or much better) for any Cartesian component and total energy per formula unit (1.5 meV or much better). Shifting the k-point grid to have a gamma point did not change the results within the precision of the convergence test performed on vacancy-free  $\text{MnO}_2$ .

Geometry optimizations were performed following the BFGS procedure (Pfrommer et al., 1997). For vacancy-free  $\text{MnO}_2$ , all cell parameters and internal ionic positions were fully relaxed. For supercells that included a vacancy, the three unit-cell angles (90°, 90°, and 120°) and the *c*-axis lattice parameter (14.001 Å) were fixed based on the vacancy-free  $\text{MnO}_2$  results, but the *a*- and *b*-axis lattice parameters and all internal ionic positions were relaxed. In the geometry optimization, the energy tolerance was 0.000005 eV/atom, and the maximum force and stress tolerance on any Cartesian component were 0.01 eV/Å and 0.02 GPa, respectively, for all  $\text{MnO}_2$  structures. Most residual force and stress values in fact were much smaller than these tolerances.

The partial density of states (DOS), which describes qualitative contribution of specific angular momentums of atoms (e.g., Mn-3*d* and O-2*p*) to the total number of electronic states corresponding to each energy level, was determined by projection of plane-wave eigenfunctions onto pseudo-atomic basis sets (Segall et al., 1996). The spilling parameter (i.e., the difference between plane-wave eigenfunctions and the projected orbitals) for the partial DOS was less than 4 %. The k-point grid for DOS calculations was 8 x 8 x 2, 4 x 4 x 2, and 2 x 2 x 2 for 1 x 1 x 1 cell, 2 x 2 x 1 supercell, and 4 x 4 x 1 supercell, respectively. The Gaussian smearing width of the DOS was 0.05 eV.

### 3. RESULTS AND DISCUSSION

#### 3.1. Geometry-optimized structures

##### 3.1.1. Interatomic distances

Table 2 shows that our spin-polarized GGA/DFT results compare favorably with available experimental values of interatomic distances in hexagonal birnessites of known vacancy content. Although the inclusion of vacancies produced significant variability among Mn-Mn [ $d(\text{Mn-Mn})$ ] and Mn-O [ $d(\text{Mn-O})$ ] distances in the birnessite sheet, the average  $d(\text{Mn-Mn})$  and  $d(\text{Mn-O})$  appear to be essentially independent of the presence of the vacancies. By contrast, inclusion of Mn vacancies changed the sheet thickness (i.e., average distance between the basal O planes in a sheet), which is reflected also in the change of O-O distance along shared (O-O<sub>sh</sub>) octahedral edges and unshared (O-O<sub>ush</sub>) edges (see Fig. 1a). An octahedron having  $O_h$  point group symmetry has  $d(\text{O-O})_{\text{sh}}/d(\text{O-O})_{\text{ush}} = 1.0$ , and deviations of this ratio from 1.0 indicate a trigonally-distorted octahedron, either compressed or elongated. The octahedra in vacancy-free birnessite sheets have a theoretical ratio of 0.88 (i.e., they are very compressed), such that each

MnO<sub>6</sub> octahedron takes on approximately a trigonally-distorted symmetry (e.g., point group  $D_{3d}$ ) instead of perfect  $O_h$  symmetry. We found that the average  $d(\text{O-O})_{\text{sh}}/d(\text{O-O})_{\text{ush}}$  ratio tends to increase, with the average  $d(\text{O-O})_{\text{sh}}$  enlarged and the average  $d(\text{O-O})_{\text{ush}}$  unchanged, as the Mn vacancy content increases (Table 2). This is in agreement with extended X-ray absorption fine structure (EXAFS) results, whereas X-ray diffraction (XRD) does not capture the change in  $d(\text{O-O})_{\text{sh}}$  (Gaillot et al., 2003; Villalobos et al., 2006). The increase of average  $d(\text{O-O})_{\text{sh}}$  with vacancy content thus indicates that a Mn vacancy elongates the compressed Mn octahedral sheet mainly along the  $c$ -axis, increasing the sheet thickness. As is well known from the Pauling Rules, when strong repulsion between Mn cations exists,  $d(\text{O-O})_{\text{sh}}$  decreases to screen the repulsion and, therefore, the increase of  $d(\text{O-O})_{\text{sh}}$  in the presence of vacancies means, as expected, that Mn-Mn repulsion is not as strong as in vacancy-free MnO<sub>2</sub>.

In the presence of vacancies, the charge-compensating H form OH groups by covalently bonding with two of O ( $\text{O}_\text{H}$ ) atoms surrounding a Mn vacancy. Hydrogen bonds are formed with two of the remaining O atoms. The OH and O-H...O bond distances are 0.98 to 0.99 Å and 2.11 to 2.17 Å respectively, and the OH bonds are oriented at a small angle (up to 10°) out of the  $a$ - $b$  plane [Fig. 1b; see also (a) in Appendix EA-2]. The interatomic distances between the H are very short: 1.73 Å in the 2 x 2 x 1 supercell and 1.88 Å in the 4 x 4 x 1 supercell. Other possible OH arrangements were explored, then compared by calculating total energies (see Appendix EA-2), but the H were found to coordinate preferentially with  $\text{O}_{2\text{Mn}}$ , as also would be expected from the Pauling Rules, and to lie just out of the  $a$ - $b$  plane in rather close proximity to one another, as shown in Fig. 1b.

### 3.1.2. Structural distortions

A Mn vacancy causes considerable local distortion of octahedra near the vacancy site through displacements of the neighboring Mn and O, although average interatomic distances remain relatively unaffected, as noted above. In the  $4 \times 4 \times 1$  supercell, two Mn positioned in the  $(1\bar{1}0)$  plane among the nearest-neighbor Mn ( $\text{Mn}_{1\text{st}}$ ) around a Mn vacancy site were displaced outward from the vacancy by  $0.10 \text{ \AA}$  as compared to their positions in vacancy-free  $\text{MnO}_2$ , but the other four Mn were displaced inward, toward the vacancy site, by  $0.07 \text{ \AA}$ . These Mn displacements led to notable variability in  $d(\text{Mn-Mn})$  around the vacancy site, from  $2.897 \text{ \AA}$  without vacancies to  $2.82 - 2.94 \text{ \AA}$  when they are present (see Appendix EA-3). In the  $2 \times 2 \times 1$  supercell, Mn relaxations were much more uniform, which is probably a consequence of the ordered vacancy superlattice created by this choice of boundary conditions.

Displacement of O around a Mn vacancy site was much more pronounced than that of the Mn. The O displacements involved a significant amount of movement along the  $c$ -axis and caused corrugation of the oxygen basal surface of the  $\text{MnO}_2$  sheet. The  $\text{O}_\text{H}$  moved outward, away from the Mn vacancy, approximately along the  $[111]$ ,  $[\bar{1}\bar{1}1]$ ,  $[11\bar{1}]$ , and  $[\bar{1}\bar{1}\bar{1}]$  directions, as compared to their positions in vacancy-free  $\text{MnO}_2$ . These outward displacements increased  $d(\text{Mn-O}_\text{H})$ , from  $1.925 \text{ \AA}$  to  $1.978 \text{ \AA}$  in the  $4 \times 4 \times 1$  supercell and from  $1.925 \text{ \AA}$  to  $1.979 \text{ \AA}$  in the  $2 \times 2 \times 1$  supercell. On the other hand, the  $\text{O}_{2\text{Mn}}$  moved relatively inward, toward the Mn vacancy, more or less along the  $[1\bar{1}\bar{1}]$  and  $[\bar{1}11]$  directions. Thus the  $\text{O}_{2\text{Mn}}$  displacements significantly decreased  $d(\text{Mn-O}_{2\text{Mn}})$ , from  $1.925 \text{ \AA}$  to  $1.852 \text{ \AA}$  in the  $4 \times 4 \times 1$  supercell and from  $1.925 \text{ \AA}$  to  $1.887 \text{ \AA}$  in the  $2 \times 2 \times 1$  supercell.

We note in passing that structural relaxation around a Mn vacancy appears to depend on the cations charge-compensating the vacancy. In the present study, at the lower vacancy content, and with a vacancy charge-compensated by four H, the  $\text{Mn}_{1\text{st}}$  and O around the vacancy undergo

both inward and outward displacements. However, in our recent study of a Zn-birnessite with the same vacancy content but with a vacancy charge-compensated by two Zn, the Mn<sub>1st</sub> all moved toward a Mn vacancy, while O around the vacancy all moved away from it (Kwon et al., 2009).

## 3.2. Electronic structure

### 3.2.1. Vacancy-free MnO<sub>2</sub>

The partial DOS exhibits spin-dependent mixing (or hybridization) mainly between Mn-3*d* and O-2*p* states (Fig. 2a), while overall the contribution of O-2*p* states is dominant in the VB and that of Mn-3*d* states is dominant in the CB. In the spin-up state, the contribution of O to the total DOS was similar to that of Mn throughout. In the spin-down state, however, the O contribution was greater than the Mn contribution to the VB, whereas Mn-3*d* states predominated over O-2*p* states in the CB. The hybridization between Mn-3*d* and O-2*p* indicated in Fig. 2a implies that the nominal O-2*p* → Mn-3*d* band gap in birnessite includes significant Mn-3*d* → Mn-3*d* transitions, as Sherman (2005) cautioned when discussing his experimental results for the band gap of triclinic birnessite.

Degenerate 3*d* orbitals of a transition metal ion such as Mn<sup>4+</sup> split into higher-energy *e<sub>g</sub>* (e.g., *d<sub>x<sup>2</sup>-y<sup>2</sup></sub>* and *d<sub>z<sup>2</sup></sub>*) and lower-energy *t<sub>2g</sub>* (e.g., *d<sub>xy</sub>*, *d<sub>yz</sub>*, and *d<sub>zx</sub>*) orbitals under octahedral coordination. Direct σ-type overlap between the transition metal *e<sub>g</sub>* orbitals and surrounding ligand *p* orbitals produces bonding (*e<sub>g</sub><sup>b</sup>*) levels and antibonding (*e<sub>g</sub><sup>\*</sup>*) levels. Moreover, π-type overlap between *t<sub>2g</sub>* orbitals and ligand *p* orbitals can give rise to bonding (*t<sub>2g</sub><sup>b</sup>*) levels and antibonding (*t<sub>2g</sub><sup>\*</sup>*) levels. Detailed orbital analysis revealed that the bands around -7 to -5 eV correspond to bonding mainly between Mn-*e<sub>g</sub>* orbitals and O-*p* orbitals (i.e., mostly *e<sub>g</sub><sup>b</sup>* levels), whereas the bands from -5 to 0 eV correspond to bonding mainly between Mn-*t<sub>2g</sub>* orbitals and O-

$p$  orbitals (i.e., mostly  $t_{2g}^b$  levels) (Fig. 2a). In particular, the bands between -1.5 to -0.5 eV, consisting of only spin-up Mn- $t_{2g}$  and O- $2p$  states, are occupied bands of the  $t_{2g}^*$  levels. Perfect high-spin Mn<sup>4+</sup> did not occur because of a slight hybridization between spin-down Mn- $3d$  states and O- $2p$  states. Nonetheless, a formal configuration of  $t_{2g}^3-e_g^0$  for Mn<sup>4+</sup> can be assigned based on a band structure wherein the three spin-down  $t_{2g}$  and two  $e_g$  states are all unoccupied and two spin-up  $e_g$  states are unoccupied (see also Appendix EA-4).

Within the spin-polarized GGA, vacancy-free MnO<sub>2</sub> has an indirect band gap of 1.3 eV [i.e., a band gap for which the minimum energy of the CB (CBM) and the maximum energy of the VB (VBM) occur at different values of the electron wavevector]; more specifically, it has an indirect 1.7 eV for spin-up states and an indirect 2.2 eV for spin-down states (see Appendix EA-4). In semiconducting materials such as those comprising Si, whose band gap also is indirect, light absorption is typically not efficient and photons mostly pass through the materials if they are not thick enough. Band gaps calculated within the GGA are well-known to be generally smaller than experimental values. Improved absolute band gap estimates may be obtained with the DFT+U approach (Anisimov et al., 1997) or the screened-exchange method (Seidl et al., 1996). Sakai et al. (2005) have reported an indirect band gap of 2.23 eV for a monolayer film of hexagonal birnessite with the chemical formula, H<sub>0.13</sub>MnO<sub>2</sub>•0.7H<sub>2</sub>O. They based their estimate on an observed linear relationship between incident photon energy and photon-to-current conversion efficiency when their sample was illuminated by visible light. The band gap was assumed to correspond to a Mn  $d-d$  transition (e.g.,  $t_{2g} \rightarrow e_g$  excitation). The chemical formula of their birnessite suggests to us that it may have contained about 0.03 Mn vacancies per octahedron, but this possibility was not examined by Sakai et al. (2005), who may in fact have considered

their sample to be vacancy-free. A full discussion of the experiments of Sakai et al. (2005) and their relevance to our DFT results has been given elsewhere (Kwon et al., 2008).

### 3.2.2. *Effects of vacancies*

Inclusion of a Mn vacancy substantially changed the electronic structure, particularly near the band-gap edges (Fig. 2 and Appendix EA-4). The DOS of hexagonal birnessite with vacancies clearly shows that the band gap narrows from 1.3 eV in vacancy-free birnessite to 0.9 eV in birnessite with 3.3 % vacancies (Fig. 2b), and then to 0.3 eV in birnessite with 12.5 % vacancies (Fig. 2c). For spin-up electrons, the band gap decreases from 1.7 eV (vacancy-free) to 1.2 eV (3.3 % vacancies), and then to 0.9 eV (12.5 % vacancies); for spin-down electrons it decreases from 2.2 eV (vacancy-free) to 2.0 eV (3.3 % vacancies), and then to 1.3 eV (12.5 % vacancies). Because the well-known band-gap underestimation by the GGA occurs mainly through a uniform downward shift of all CBs (which can differ for spin-up and spin-down states), it should not affect the accuracy of our calculated band gap trend for different vacancy contents. Band gap reduction by Mn vacancies would promote formation of more pairs of photo-induced electrons and holes upon illumination. Furthermore, while the band gap for spin-down electrons in vacancy-free  $\text{MnO}_2$  is indirect, that for  $\text{MnO}_2$  with vacancies is direct (i.e., they exhibit a band gap for which the CBM and the VBM occur at the same value of the electron wavevector, see Appendix EA-4). This appearance of a direct band gap implies that light absorption would be more efficient in  $\text{MnO}_2$  with vacancies than in vacancy-free  $\text{MnO}_2$ .

The substantial band-gap reduction by a Mn vacancy is due to the introduction of states at the top of the VB, while O-2*p* and Mn-3*d* hybridization occurs similarly to that in vacancy-free  $\text{MnO}_2$ . These newly-introduced states (around -1 to 0 eV in Fig. 2b, c) are contributed almost entirely by the nearest-neighbor Mn and O atoms around a vacancy. In particular, the

states can be attributed mostly to Mn-3*d* states and O<sub>2Mn</sub>-2*p* states around a vacancy, the latter of which are oriented parallel to the axial Mn-O bonds in the MnO<sub>6</sub> octahedra and exist as a consequence of the Mn-O bonds lost by removal of Mn<sup>4+</sup> to create a vacancy.

### **3.3. Enhancement of photoreactivity**

Our DFT calculations show that the semiconductor band gap in hexagonal birnessite is both reduced in magnitude and becomes direct in the presence of Mn vacancies, which are characteristic defects in all synthetic and natural birnessites investigated experimentally to date, leading us to propose that these vacancies promote the photoreduction of natural birnessites in aquatic systems. Sakai et al. (2005) reported apparently the first observation of photocurrent generation by a chemically-synthesized hexagonal birnessite that we estimate to contain about 3 % vacancies. A monolayer film of this material produced photocurrents under visible light radiation ( $\lambda < 500$  nm) without significant structural decomposition. Matsunaga et al. (1995) observed rapid photoreduction of  $\delta$ -MnO<sub>2</sub>, a chemically-synthesized hexagonal birnessite which is known to contain about 6 % Mn vacancies (Villalobos et al., 2003, 2006), that was suspended in seawater containing organic acids characteristic of phytoplankton blooms and then subjected to sunlight illumination. These two experimental findings indirectly support our hypothesis about the importance of Mn vacancies to the photoreactivity of hexagonal birnessite.

The photoreduction of birnessite is not only determined by the band gap, which is decreased in the presence of Mn vacancies, but also the recombination rate of the electrons and holes produced by illumination. Rapid recombination of these photon-generated charge-carriers diminishes the possibility of subsequent electron-transfer processes (Grätzel, 2001) and, therefore, efficient separation of the charge-carriers after excitation enhances the opportunity for the two-electron reduction from Mn(IV) to Mn(II) (Gilbert and Banfield, 2005). Introduced

states that decrease the band gap often also diminish the photoreactivity of semiconducting materials because they are localized deep inside the band gap and so function as recombination centers, or traps, of the generated charge-carriers [e.g., the  $d$  states of transition metals doped into  $\text{TiO}_2$  (Choi et al., 1994)]. In the present case, however, Figure 2 shows that the CB in the presence of a Mn vacancy is negligibly different from that in vacancy-free  $\text{MnO}_2$ , and Appendix EA-4 shows that the states introduced by a Mn vacancy have a finite bandwidth overlapping the band states of vacancy-free  $\text{MnO}_2$ . Therefore, we propose that band-gap reduction by a Mn vacancy would not significantly lower the mobility of photo-induced charge carriers. In addition, Sakai et al. (2005) speculated that the nanoscale thickness ( $< 1$  nm) of the birnessite film they investigated facilitated excited electron and hole escape before recombination could occur.

Qualitatively, efficient electron-hole separation by a Mn vacancy is evident from comparing the charge distribution (i.e., electronic orbitals) at the VBM and the CBM in the absence and presence of vacancies (Fig. 3). Electronic transitions from the VB to the CB upon illumination would most likely leave hole states at the VBM and excited electron states at the CBM. In vacancy-free  $\text{MnO}_2$ , most of the electron and hole states are overlapping (Fig. 3a, b). In the presence of a vacancy, however, the electron and hole states are well-separated (Fig. 3c, d), i.e., the VBM hole states are near the vacancy site, whereas the CBM electronic states are mostly in a neighboring sheet, well away from the VBM hole states. The lowest CB electronic states near a vacancy site are found at *ca.* 0.2 eV ( $4 \times 4 \times 1$  supercell) and 0.3 eV ( $2 \times 2 \times 1$  supercell) above the CBM at the  $\Gamma$  point, indicating that efficient charge separation would persist at ambient temperature. Further research to compute the matrix elements for electronic transitions (You and Cardona, 2005) in the absence and presence of Mn vacancies may provide more conclusive insights on the recombination rate.

## ACKNOWLEDGMENTS

This research reported in this paper was supported by the Director, Office of Energy Research, Office of Basic Energy Sciences, of the U.S. Department of Energy under Contract No. DE-AC02-05CH11231. Our computations used resources of the National Energy Research Scientific Computing Center, which is supported by the Office of Science of the U.S. Department of Energy under contract No. DE-AC02-05CH11231. We acknowledge the use of the SCARF computing facilities at STFC Rutherford Appleton Laboratory.

## REFERENCES

- Anisimov V. I., Aryasetiawan F., and Lichtenstein A. I. (1997) First-principles calculations of the electronic structure and spectra of strongly correlated systems: The LDA+U method. *J. Phys. Condens. Matter* **9**, 767-808.
- Asahi R., Morikawa T., Ohwaki T., Aoki K., and Taga Y. (2001) Visible-light photocatalysis in nitrogen-doped titanium oxides. *Science* **293**, 269-271.
- Balachandran D., Morgan D., Ceder G., and van de Walle A. (2003) First-principles study of the structure of stoichiometric and Mn-deficient MnO<sub>2</sub>. *J. Solid State Chem.* **173**, 462-475.
- Bargar J., Webb S. M., and Tebo B. M. (2005) EXAFS, XANES and *in-situ* SR-XRD characterization of biogenic manganese oxides produced in sea water. *Phys. Scr.* **T115**, 888-890.
- Choi W., Termin A., and Hoffmann M. R. (1994) The role of metal ion dopants in quantum-sized TiO<sub>2</sub>: Correlation between photoreactivity and charge carrier recombination dynamics. *J. Phys. Chem.* **98**, 13669-13679.
- Clark S. J., Segall M. D., Pickard, C. J., Hasnip, P. J., Probert, M. J., Refson, K., and Payne, M. C. (2005) First principles methods using CASTEP. *Z. Kristallogr.* **220**, 567-570.
- Delgadillo-Hinojosa F., Segovia-Zavala J. A., Huerta-Díaz M. A., and Atilano-Silva H. (2006) Influence of geochemical and physical processes on the vertical distribution of manganese in Gulf of California waters. *Deep-Sea Res. Part I* **53**, 1301-1319.
- Drits V. A., Silvester E., Gorshkov A. I., and Manceau A. (1997) Structure of synthetic monoclinic Na-rich birnessite and hexagonal birnessite .1. Results from X-ray diffraction and selected-area electron diffraction. *Am. Mineral.* **82**, 946-961.
- Gaillot A. C., Flot D., Drits V. A., Manceau A., Burghammer M., and Lanson B. (2003) Structure of synthetic K-rich birnessite obtained by high-temperature decomposition of KMnO<sub>4</sub>. I. Two-layer polytype from 800 °C experiment. *Chem. Mater.* **15**, 4666-4678.
- Gilbert B. and Banfield J. F. (2005) Molecular-scale processes involving nanoparticulate minerals in biogeochemical systems. In *Molecular Geomicrobiology* (eds. J. F. Banfield,

- J. Cervini-Silva, and K. H. Nealson). Vol. **59**, Mineralogical Society of America, Chantilly. pp. 109-155.
- Grätzel M. (2001) Photoelectrochemical cells. *Nature* **414**, 338-344.
- Hwang H. Y. (2005) Perovskites - Oxygen vacancies shine blue. *Nat. Mater.* **4**, 803-804.
- Justicia I., Ordejon P., Canto G., Mozos J. L., Fraxedas J., Battiston G. A., Gerbasi R., and Figueras A. (2002) Designed self-doped titanium oxide thin films for efficient visible-light photocatalysis. *Advanced Materials* **14**, 1399-1402.
- Kohn W. and Sham L. J. (1965) Self-consistent equations including exchange and correlation effects. *Phys. Rev.* **140**, A1133-A1138.
- Kresse G. and Furthmüller J. (1996) Efficient iterative schemes for ab initio total-energy calculations using a plane-wave basis set. *Phys. Rev. B* **54**, 11169-11186.
- Kwon K. D., Refson K., and Sposito G. (2008) Defect-induced photoconductivity in layered manganese oxides: A density functional theory study. *Phys. Rev. Lett.* **100**, 146601.
- Lanson B., Drits V. A., Feng Q., and Manceau A. (2002) Structure of synthetic Na-birnessite: Evidence for a triclinic one-layer unit cell. *Am. Mineral.* **87**, 1662-1671.
- Landing W. M. and Bruland K. W. (1987) The contrasting biogeochemistry of iron and manganese in the Pacific Ocean. *Geochim. Cosmochim. Acta* **51**, 29-43.
- Manceau A., Lanson B., and Drits V. A. (2002) Structure of heavy metal sorbed birnessite. Part III: Results from powder and polarized extended X-ray absorption fine structure spectroscopy. *Geochim. Cosmochim. Acta* **66**, 2639-2663.
- Manceau A., Lanson M., and Geoffroy N. (2007) Natural speciation of Ni, Zn, Ba, and As in ferromanganese coatings on quartz using X-ray fluorescence, absorption, and diffraction. *Geochim. Cosmochim. Acta* **71**, 95-128.
- Matsunaga K., Ohyama T., Kuma K., Kudo I., and Suzuki Y. (1995) Photoreduction of manganese dioxide in seawater by organic substances under ultraviolet or sunlight. *Water Res.* **29**, 757-759.
- Moessner R. and Ramirez A. R. (2006) Geometrical frustration. *Physics Today* **59**, 24-29.
- Monkhorst H. J. and Pack J. D. (1976) Special points for Brillouin-zone integrations. *Phys. Rev. B* **13**, 5188-5192.
- Morgan J. J. (2000) Manganese in natural waters and earth's crust: Its availability to organisms. In *Metal Ions in Biological Systems* (eds. A. Sigel and H. Sigel). Vol. **37**, Marcel Dekker, Inc., New York. pp. 1-34.
- Nolan M. and Elliott S. D. (2006) The p-type conduction mechanism in Cu<sub>2</sub>O: A first principles study. *Phys. Chem. Chem. Phys.* **8**, 5350-5358.
- Pask J. E., Singh D. J., Mazin I. I., Hellberg C. S., and Kortus J. (2001) Structural, electronic, and magnetic properties of MnO. *Phys. Rev. B* **64**, 024403.
- Payne M. C., Teter M. P., Allan D. C., Arias T. A., and Joannopoulos, J. D. (1992) Iterative minimization techniques for *ab initio* total-energy calculations: Molecular dynamics and conjugate gradients. *Rev. Mod. Phys.* **64**, 1045-1097.
- Perdew J. P., Burke K., and Ernzerhof M. (1996) Generalized gradient approximation made simple. *Phys. Rev. Lett.* **77**, 3865-3868.
- Pfrommer B. G., Cote M., Louie S. G., and Cohen M. L. (1997) Relaxation of crystals with the quasi-Newton method. *J. Comput. Phys.* **131**, 233-240.
- Picozzi S., Ma C., Yang Z., Bertacco R., Cantoni M., Cattoni A., Petti D., Brivio S., and Ciccacci F. (2007) Oxygen vacancies and induced changes in the electronic and magnetic

- structures of  $\text{La}_{0.66}\text{Sr}_{0.33}\text{MnO}_3$ : A combined *ab initio* and photoemission study. *Phys. Rev. B* **75**, 094418-11.
- Sakai N., Ebina Y., Takada K., and Sasaki T. (2005) Photocurrent generation from semiconducting manganese oxide nanosheets in response to visible light. *J. Phys. Chem. B* **109**, 9651-9655.
- Saratovsky I., Wightman P. G., Pastén P. A., Gaillard J. F., and Poeppelmeier K. R. (2006) Manganese oxides: Parallels between abiotic and biotic structures. *J. Am. Chem. Soc.* **128**, 11188-11198.
- Segall M. D., Shah R., Pickard C. J., and Payne M. C. (1996) Population analysis of plane-wave electronic structure calculations of bulk materials. *Phys. Rev. B* **54**, 16317-16320.
- Segall M. D., Lindan, P. J. D., Probert M. J., Pickard C. J., Hasnip P. J., Clark S. J., and Payne M. C. (2002) wFirst-principles simulation: Ideas, illustrations and the CASTEP code. *J. Phys. Condens. Matter.* **14**, 2717-2744.
- Seidl A., Görling A., Vogl P., Majewski J. A., and Levy M. (1996) Generalized Kohn-Sham schemes and the band-gap problem. *Phys. Rev. B* **53**, 3764-3774.
- Sherman D. M. (2005) Electronic structures of iron(III) and manganese(IV) (hydr)oxide minerals: Thermodynamics of photochemical reductive dissolution in aquatic environments. *Geochim. Cosmochim. Acta* **69**, 3249-3255.
- Silvester E., Manceau A., and Drits V. A. (1997) Structure of synthetic monoclinic Na-rich birnessite and hexagonal birnessite .2. Results from chemical studies and EXAFS spectroscopy. *Am. Mineral.* **82**, 962-978.
- Singh D. J. (1997) Magnetic and electronic properties of  $\text{LiMnO}_2$ . *Phys. Rev. B* **55**, 309-312.
- Spokes L. J. and Liss P. S. (1995) Photochemically induced redox reactions in seawater, I. Cations. *Mar. Chem.* **49**, 201-213.
- Sunda W. G. and Huntsman S. A. (1988) Effect of sunlight on redox cycles of manganese in the southwestern Sargasso Sea. *Deep-Sea Res. Part A* **35**, 1297-1317.
- Sunda W. G. and Huntsman S. A. (1990) Diel cycles in microbial manganese oxidation and manganese redox speciation in coastal waters of the Bahama Islands. *Limnol. Oceanogr.* **35**, 325-338.
- Sunda W. G. and Huntsman S. A. (1994) Photoreduction of manganese oxides in seawater. *Mar. Chem.* **46**, 133-152.
- Sunda W. G., Huntsman S. A., and Harvey G. R. (1983) Photoreduction of manganese oxides in seawater and its geochemical and biological implications. *Nature* **301**, 234-236.
- Takahashi Y., Manceau A., Geoffroy N., Marcus M. A., and Usui A. (2007) Chemical and structural control of the partitioning of Co, Ce, and Pb in marine ferromanganese oxides. *Geochim. Cosmochim. Acta* **71**, 984-1008.
- Tebo B. M., Bargar J. R., Clement B. G., Dick G. J., Murray K. J., Parker D., Verity R., and Webb S. M. (2004) Biogenic manganese oxides: Properties and mechanisms of formation. *Annu. Rev. Earth Planet. Sc.* **32**, 287-328.
- Toner B., Manceau A., Webb S. M., and Sposito G. (2006) Zinc sorption to biogenic hexagonal-birnessite particles within a hydrated bacterial biofilm. *Geochim. Cosmochim. Acta* **70**, 27-43.
- Vanderbilt D. (1990) Soft self-consistent pseudopotentials in a generalized eigenvalue formalism. *Phys. Rev. B* **41**, 7892-7895.

- Villalobos M., Toner B., Bargar J., and Sposito G. (2003) Characterization of the manganese oxide produced by *Pseudomonas putida* strain MnB1. *Geochim. Cosmochim. Acta* **67**, 2649-2662.
- Villalobos M., Bargar J., and Sposito G. (2005) Mechanisms of Pb(II) sorption on a biogenic manganese oxide. *Environ. Sci. Technol.* **39**, 569-576.
- Villalobos M., Lanson B., Manceau A., Toner B., and Sposito G. (2006) Structural model for the biogenic Mn oxide produced by *Pseudomonas putida*. *Am. Mineral.* **91**, 489-502.
- Viswanatha R., Sapra S., Satpati B., Satyam P. V., Dev B. N., and Sarma D. D. (2004) Understanding the quantum size effects in ZnO nanocrystals. *J. Mater. Chem.* **14**, 661-668.
- Waite T. D. and Szymczak R. (1993) Manganese dynamics in surface waters of the Eastern Caribbean. *J. Geophys. Res.* **98**, 2361-2369.
- Waite T. D., Wrigley I. C., and Szymczak R. (1988) Photoassisted dissolution of a colloidal manganese oxide in the presence of fulvic-acid. *Environ. Sci. Technol.* **22**, 778-785.
- Wang Y. and Doren D. J. (2005) First-principles calculations on TiO<sub>2</sub> doped by N, Nd, and vacancy. *Solid State Commun.* **136**, 186-189.
- Webb S. M., Tebo B. M., and Bargar J. R. (2005) Structural characterization of biogenic Mn oxides produced in seawater by the marine *bacillus sp* strain SG-1. *Am. Mineral.* **90**, 1342-1357.
- Yang G., Zhao X., and Qi J. (2003) Advances in the marine photochemistry of some important transition metal elements. *J. Ocean Univ. Qingdao* **2**, 79-84.
- Yu P. Y. and Cardona M. (2005) *Fundamentals of Semiconductors*. Springer, New York.

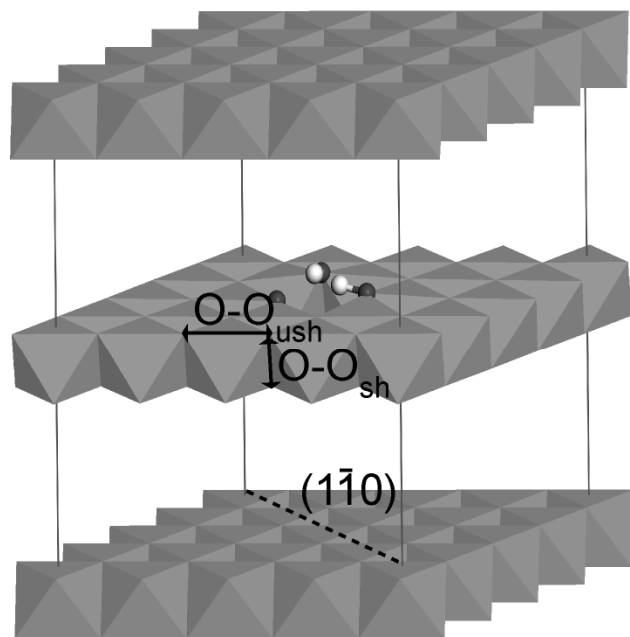
## Figure Captions

Fig.1. Geometry-optimized structures of (a)  $4 \times 4 \times 1$   $\text{MnO}_2$  supercell containing a Mn vacancy (3.3 % vacancies) and (b) its middle sheet containing the vacancy projected onto the  $a$ - $b$  plane. Double-headed arrows indicate (a) O-O distances along shared ( $\text{O-O}_{\text{sh}}$ ) and unshared ( $\text{O-O}_{\text{ush}}$ ) Mn octahedral edges and (b) distances between Mn and O.

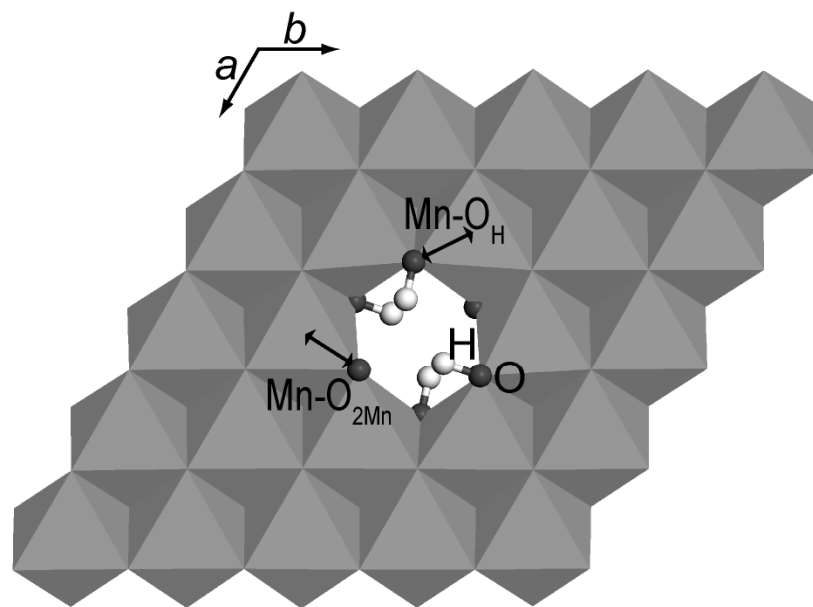
Fig. 2. Density of states (DOS) of (a) vacancy-free  $\text{MnO}_2$  (unit cell) with its O- $2p$  and Mn- $3d$  contribution to the total DOS. Total DOS of  $\text{MnO}_2$  with vacancies (filled areas) in (b)  $4 \times 4 \times 1$  supercell and (c)  $2 \times 2 \times 1$  supercell, with the corresponding total DOS of vacancy-free  $\text{MnO}_2$  (solid lines). Negative energy states are the electron-occupied valence band (VB), and positive energy states are the unoccupied conduction band (CB). Double-headed arrows represent the band gap, which is the energy difference between the maximum energy of the VB (VBM) and the minimum energy of the CB (CBM). The vertical dotted line represents the mean energy level between the VBM and the CBM of (a) vacancy-free  $\text{MnO}_2$  and (b, c)  $\text{MnO}_2$  with vacancies. In (b) and (c), the CBM of vacancy-free  $\text{MnO}_2$  was aligned at the CBM of  $\text{MnO}_2$  with vacancies.

Fig. 3. Charge distributions of (a) VBM hole states (light gray) and (b) CBM electron states (dark gray) in vacancy-free  $\text{MnO}_2$  ( $4 \times 4 \times 1$  supercell), and (c) VBM hole states (light gray) and (d) CBM electron states (dark gray) in  $\text{MnO}_2$  with vacancies ( $4 \times 4 \times 1$  supercell). Isosurfaces represent  $0.001 \text{ e}^-/\text{\AA}^3$ .

Fig. 1



(a)



(b)

Fig. 2

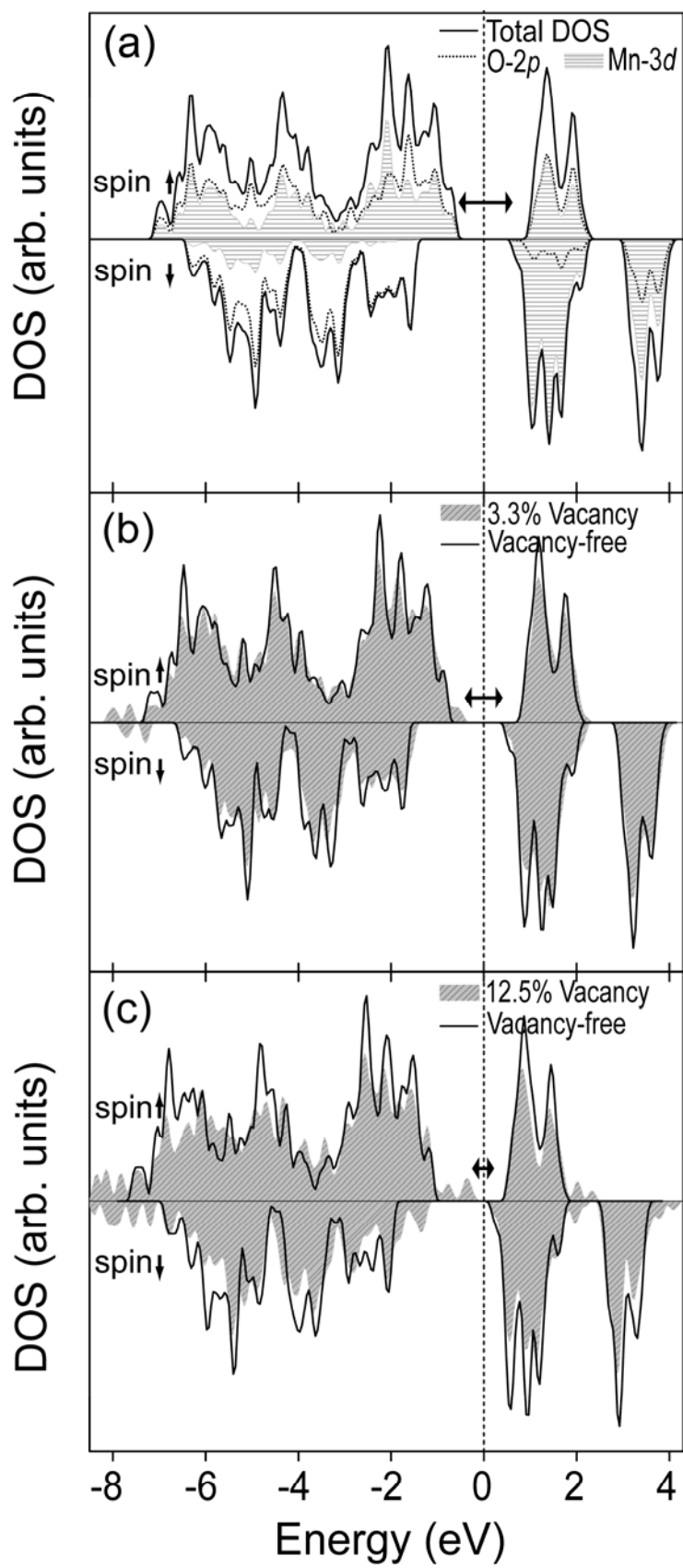


Fig. 3

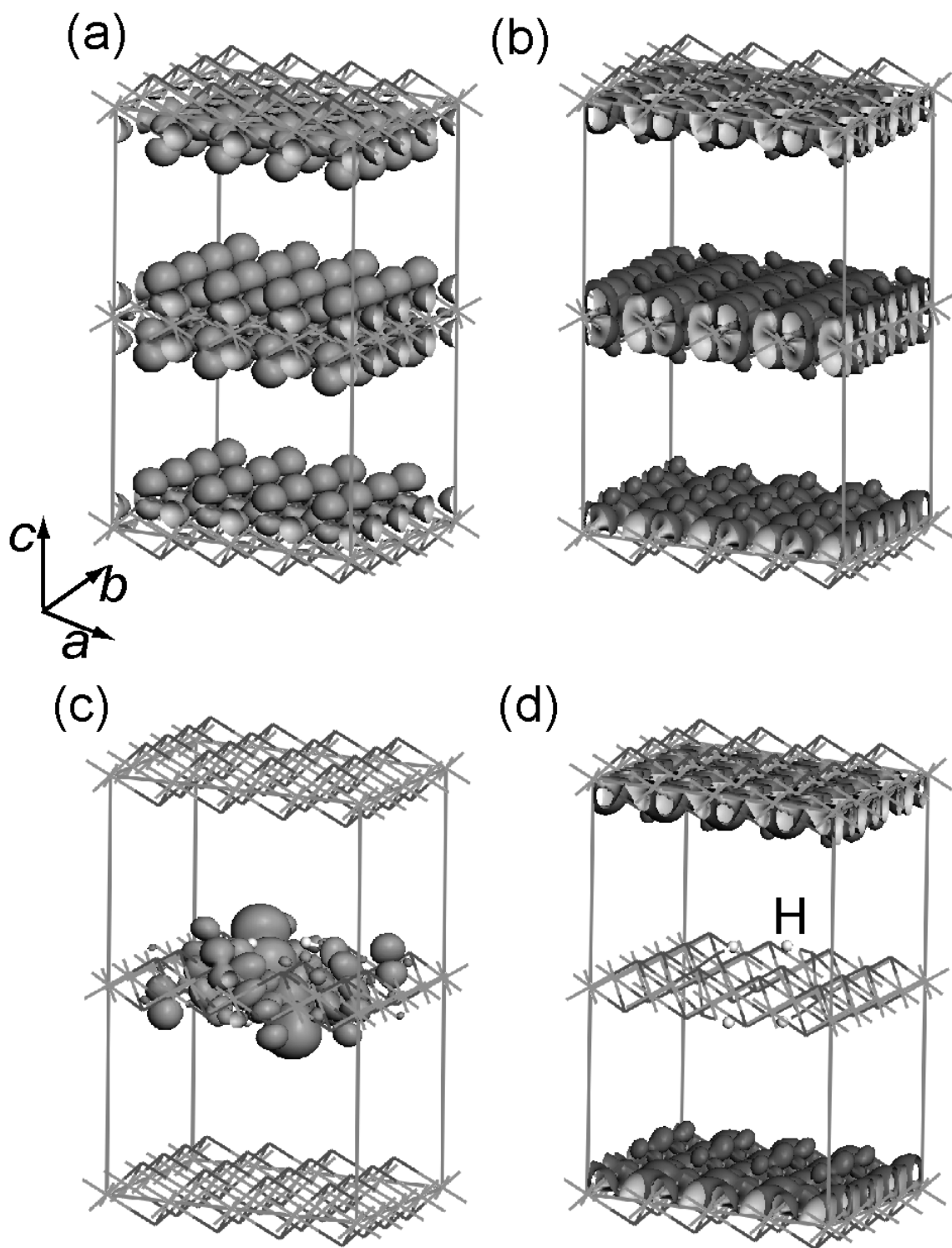


Table 1 Interatomic distances and  $c$  lattice parameter ( $\text{\AA}$ ) in vacancy-free hexagonal layer type  $\text{Mn(IV)O}_2$  as predicted by DFT geometry optimization without (nsp) or with (sp) spin polarization.

| Distance | DFT-nsp | DFT-sp |
|----------|---------|--------|
| Mn-Mn    | 2.788   | 2.897  |
| Mn-O     | 1.893   | 1.925  |
| $c$      | 14.337  | 14.001 |

Table 2 Structural parameters for geometry-optimized hexagonal birnessite. The vacancy content per octahedron is indicated at the top of each column of data. Values in parentheses are averages.

| Distance (Å)                                       | DFT   |                          |                          | Experiment       |                    |                  |                  |                    |
|--|-------|--------------------------|--------------------------|------------------|--------------------|------------------|------------------|--------------------|
|  | 0     | 0.033                    | 0.125                    | 0.06             |                    | 0.115            |                  |                    |
|  |       |                          |                          | XRD <sup>a</sup> | EXAFS <sup>a</sup> | XRD <sup>b</sup> | XRD <sup>c</sup> | EXAFS <sup>c</sup> |
| Mn-Mn  | 2.897 | 2.820 – 2.943<br>(2.895) | 2.895                    | 2.84             | 2.88               | 2.840            | 2.845            | 2.87               |
| Mn-O   | 1.925 | 1.852 – 1.978<br>(1.925) | 1.887 – 1.979<br>(1.925) | 1.92             | 1.90               | 1.914            | 1.925            | 1.91               |
| Mn sheet thickness                                 | 1.91  | 1.94                     | 2.02                     | 2.00             | 1.84               | 1.96             | 2.00             | 1.90               |
| O-O <sub>sh</sub> <sup>d</sup>                     | 2.54  | 2.56                     | 2.63                     | 2.58             | 2.48               | 2.57             | 2.59             | 2.52               |
| O-O <sub>ush</sub> <sup>d</sup>                    | 2.90  | 2.90                     | 2.90                     | 2.84             | 2.88               | 2.84             | 2.85             | 2.87               |
| O-O <sub>sh</sub> /O-O <sub>ush</sub> <sup>e</sup> | 0.88  | 0.88                     | 0.91                     | 0.91             | 0.86               | 0.90             | 0.91             | 0.88               |

<sup>a</sup> Nanoparticle  $\delta$ -MnO<sub>2</sub> with structural formula Na<sub>0.24</sub>[Mn(IV)<sub>0.94</sub>□<sub>0.06</sub>]O<sub>2</sub>·0.72H<sub>2</sub>O (Villalobos et al., 2006).

<sup>b</sup> Microcrystalline layer type K-MnO<sub>2</sub> with the structural formula K<sub>0.231</sub>Mn(III)<sub>0.077</sub>[Mn(IV)<sub>0.885</sub>□<sub>0.115</sub>]O<sub>2</sub>·0.60H<sub>2</sub>O (Gaillot et al., 2003).

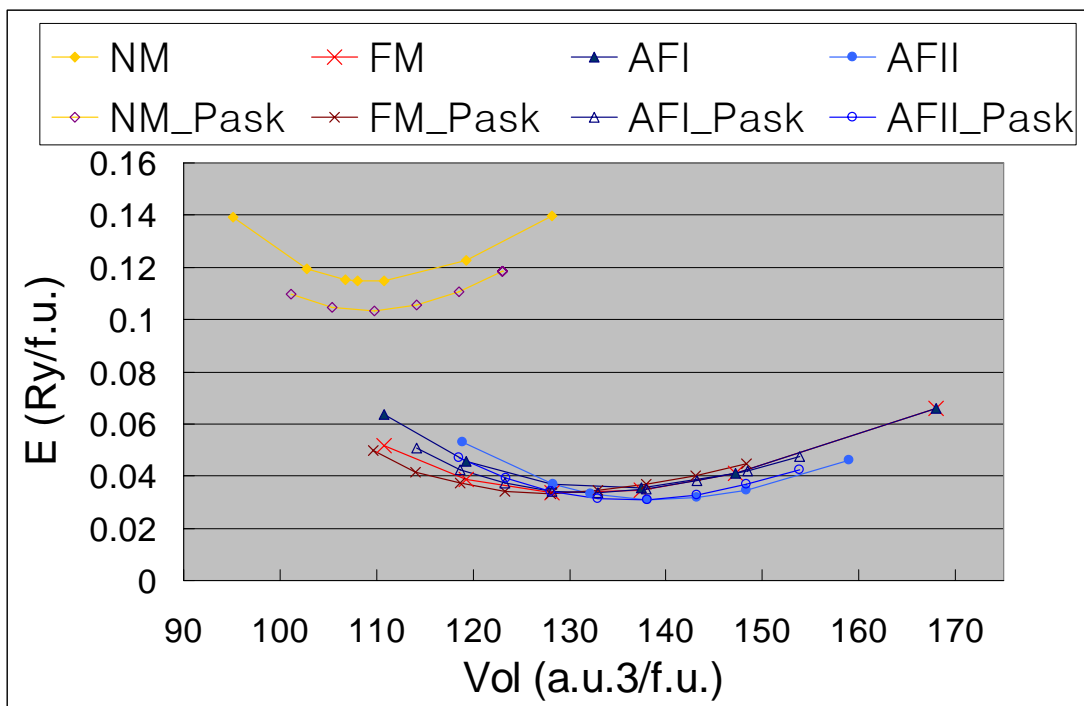
<sup>c</sup> A powder sample of layer type K-MnO<sub>2</sub> (Gaillot et al., 2003).

<sup>d</sup> Average distance along shared (O-O<sub>sh</sub>) and unshared (O-O<sub>ush</sub>) octahedral edges. In the DFT supercell having 0.033 vacancy content,  $d(\text{O-O})_{\text{sh}}$  varied at 2.53 – 2.85 Å,  $d(\text{O-O})_{\text{ush}} = 2.71 – 2.98$  Å for occupied octahedra, and  $d(\text{O-O})_{\text{sh}}$  varied at 2.74 – 2.85 Å,  $d(\text{O-O})_{\text{ush}} = 3.05 – 3.33$  Å for an empty octahedron (see Appendix EA-3).

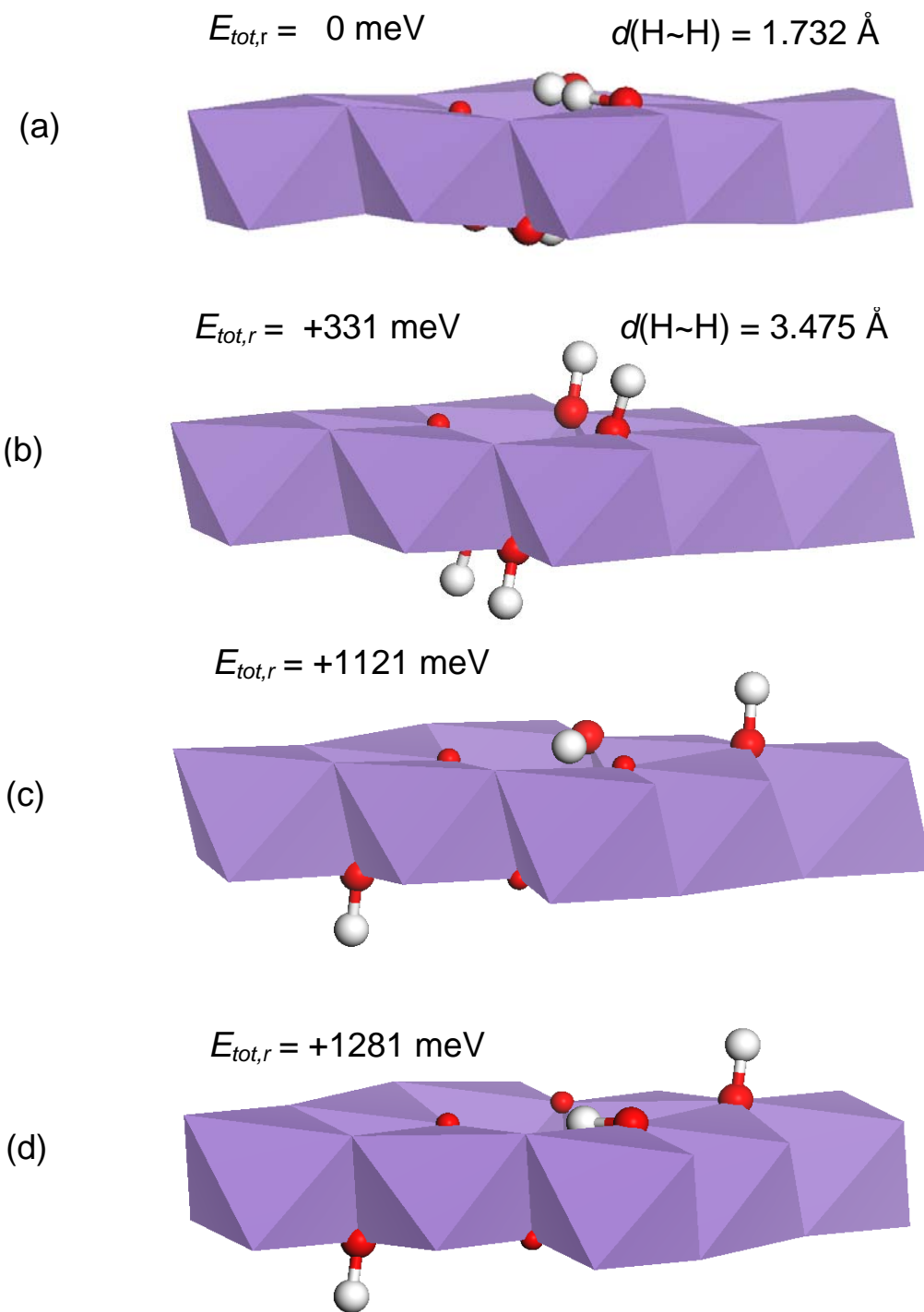
<sup>e</sup> Undistorted octahedra would yield 1.00 for this ratio.

## Appendix A. Supplementary data

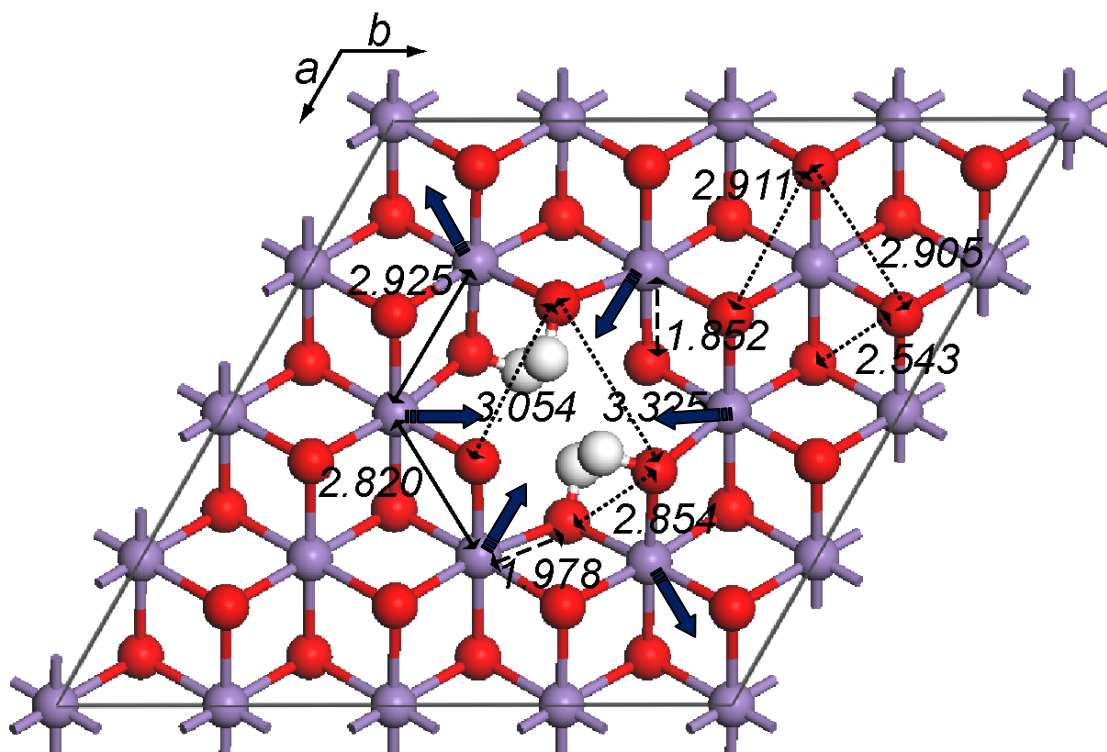
EA-1. MnO structure and total energy comparison between calculated with the pseudopotentials used in this study and calculated using the all-electron method of Pask et al. (2001) *Physical Review B*, 64, 024403. NM: non-magnetic; FM: ferromagnetic; AFI: antiferromagnetic with [001] direction; AFII: antiferromagnetic with [111] direction.



EA-2. Geometry-optimized structures of a protonated Mn vacancy defect as influenced by different H positions in the  $2 \times 2 \times 1$  supercell: (a) H with its OH nearly parallel to the  $a$ - $b$  plane, (b) H with its OH perpendicular to the sheet, (c) H at the vacancy as well as at O bonded to three Mn ( $O_{3Mn}$ ), and (d) H at an isomeric position of (c).  $E_{tot,r}$  is total energy relative to the energy of the structure in (a).



EA-3. Interatomic distances ( $\text{\AA}$ ) around a protonated Mn vacancy in  $4 \times 4 \times 1$   $\text{MnO}_2$  supercell. Solid double-head arrows represent distances between Mn and Mn; dotted one represent distances between O and O; dashed ones represent distances between Mn and O. Thick one-head arrows represent displacement directions of atoms compared to their positions in vacancy-free  $\text{MnO}_2$ . Purple: Mn; Red: O; White: H.



EA-4. Band structures of (a) vacancy-free  $\text{MnO}_2$  (unit cell), (b) vacancy-free  $\text{MnO}_2$  ( $2 \times 2 \times 1$  supercell), and (c)  $\text{MnO}_2$  with 12.5 % vacancies ( $2 \times 2 \times 1$  supercell) [adapted from Kwon et al. (2008) *Phys. Rev. Lett.* **100**, 146601]. Double-headed arrows indicate the band gap in (b) and (c). Solid lines and dashed lines are energy bands for spin-up and spin-down electrons, respectively. Negative energy levels correspond to the electron-occupied valence band (VB), and positive energy levels correspond to the unoccupied conduction band (CB). The mean energy level between the VBM and the CBM was set equal to zero. Greek and Roman letters represent high-symmetry points which electron wavevectors take on in the first Brillouin zone of hexagonal  $\text{MnO}_2$ . Stars (\*) in (c) indicate a direct band gap for spin-down electrons at the  $\Gamma$  point.

